THE JOURNAL OF BIOLOGICAL CHEMISTRY VOL. 287, NO. 50, pp. 42053–42063, December 7, 2012

The p53-induced Gene *Ei24* Is an Essential Component of the Basal Autophagy Pathway*[S]

Received for publication, September 4, 2012, and in revised form, October 14, 2012 Published, JBC Papers in Press, October 16, 2012, DOI 10.1074/jbc.M112.415968

Yan G. Zhao[‡§], Hongyu Zhao[‡§], Lin Miao[§], Li Wang[‡], Fei Sun[‡], and Hong Zhang[‡§1]

From the [‡]State Key Laboratory of Biomacromolecules, Institute of Biophysics, Chinese Academy of Sciences, 100101 Beijing, P.R. China and the [§]National Institute of Biological Sciences, 102206 Beijing, P.R. China

Background: The function of the p53-induced gene *Ei24* in the autophagy pathway remains largely unknown.
Results: *Ei24* deficiency impairs autophagic flux. Mice deficient in *Ei24* show massive neuron degeneration and severe liver injury.
Conclusion: *Ei24* functions in basal autophagy in clearance of aggregate-prone proteins in neurons and hepatocytes.
Significance: We revealed that EI24 is an essential component of the basal autophagy pathway.

Ei24 **is a DNA damage response gene involved in growth suppression and apoptosis. The physiological function of** ***Ei24*****, however, is poorly understood. Here we generated conditional knock-out mice of** ***Ei24*** **and demonstrated that EI24 is an essential component of the basal autophagy pathway. Mice with neural-specific** ***Ei24*** **deficiency develop age-dependent neurological abnormalities caused by massive axon degeneration and extensive neuron loss in brain and spinal cord. Notably, ablation of** ***Ei24*** **leads to vacuolated oligodendroglial cells and demyelination of axons. Liver-specific depletion of** ***Ei24*** **causes severe hepatomegaly with hepatocyte hypertrophy.** ***Ei24*** **deficiency impairs autophagic flux, leading to accumulation of LC3, p62 aggregates, and ubiquitin-positive inclusions. Our study indicates that** ***Ei24*** **is an essential autophagy gene and plays an important role in clearance of aggregate-prone proteins in neurons and hepatocytes.**

Ei24 (etoposide-induced 2.4 kb transcript),[2] also known as *PIG8* (p53-induced gene 8), encodes an ER-localized six transmembrane protein, expression of which is highly induced by the tumor suppressor protein p53 (1–3). Overexpression of *Ei24* suppresses cell growth and induces apoptosis, while depletion of *Ei24* results in suppression of apoptosis in response to pro-apoptotic treatment (2–4). The human *EI24* gene is located on chromosome 11q23, a region frequently displaying loss of heterozygosity in several malignancies, including invasive cervical cancers, breast carcinomas and malignant melanoma (5). The tumor suppression function of *Ei24* is further substantiated by reduced expression in invasive breast cancers (3, 5). However, the physiological function of *Ei24* is still poorly understood.

Autophagy is an evolutionarily conserved intracellular catabolic system, involving the formation of a closed double-membrane autophagosome and its subsequent delivery to the vacuole/lysosome for degradation (6, 7). Under normal physiological conditions, autophagy occurs at a basal constitutive level, removing misfolded, or aggregate-prone proteins and damaged organelles (8). The homeostatic function of basal autophagy plays an important role in neuronal protection and tumor suppression in mammals (8, 9). Neural-specific knockout of *Atg7* or *Atg5* (genes essential for autophagosome formation) causes dramatic accumulation of autophagy substrates such as p62 (also known as sequestosome 1, SQSTM1) and ubiquitin-positive aggregates in neurons, accompanied by massive neuron degeneration in various brain regions (10–12). The autophagy gene *beclin 1* is a haploinsufficient tumor suppressor (8). *Atg7* and *Atg5* deficiency in liver cause hepatomegaly and subsequently multiple liver adenomas (13, 14). The tumor suppression function of autophagy is at least partially attributed to its elimination of p62, accumulation of which leads to persistent activation of the Nrf2 stress response and dysregulation of NF-κB signaling (14–16).

A group of evolutionarily conserved Atg proteins has been identified from yeast genetic studies that act at distinct steps of autophagosome formation (6, 7). In mammalian cells, however, the autophagy process involves more complex membrane dynamics (17). The endoplasmic reticulum (ER), Golgi apparatus, recycling endosomes, and plasma membrane all contribute to autophagosomal membranes in mammalian cells (18, 19). Among them, PI(3)P-enriched subdomains of the ER, called omegasomes, provide a platform for recruiting Atg proteins and subsequent autophagosome formation (18). The more elaborate autophagic machinery in higher eukaryotes requires Atg proteins and also metazoan-specific autophagy components. Genetic screens in *Caenorhabditis elegans* identified *epg-4*, the *Ei24* homolog, as an essential autophagy gene, loss of function of which causes defective autophagic degradation of a variety of protein aggregates during embryogenesis (20). *epg-4* regulates progression of omegasomes to autophagosomes (20). *Ei24* is also essential for starvation-induced autophagy (20). Distinct from the role of *epg-4* at the early step of autophagosome formation in *C. elegans*, knockdown of *Ei24* by siRNA results in accumulation of degradation-defective autolysosomes (20).

---

* This work was supported by the National Basic Research Program of China (2011CB910100, 2010CB835201) (to H. Z.).

[S] This article contains supplemental Figs. S1–S4 and movie.

[1] To whom correspondence should be addressed. Tel.: 86.10.80728590; Fax: 86.10.80727517; E-mail: hongzhang@sun5.ibp.ac.cn.

[2] The abbreviations used are: *Ei24*, etoposide-induced 2.4 kb transcript; SQSTM, sequestosome; AMC, aminomethylcoumarin; MBP, myelin basic protein; H&E, hematoxylin and eosin; DCN, deep cerebellar nuclei.

Here we generated mice with tissue-specific deficiency of *Ei24*. Neural-specific *Ei24*-deficient mice exhibit massive axonal degeneration and neuronal cell loss in various brain and spinal cord regions. *Ei24* deficiency causes vacuolation of oligodendroglial cells. Liver-specific *Ei24*-deficient mice have hepatocellular enlargement and hepatomegaly. *Ei24* deficiency impairs autophagic flux, leading to accumulation of LC3, p62 aggregates, and ubiquitin-positive inclusions. Our study demonstrates that *Ei24* is an essential component of basal autophagy in removing aggregate-prone proteins.

EXPERIMENTAL PROCEDURES

Mice—To construct the *Ei24* targeting allele, exon 3 of *Ei24* was flanked by two loxP sequences and a neomycin phosphotransferase expression cassette. The targeting vector was electroporated into 129 R1 embryonic stem (ES) cells. Three homologous recombinants were identified by Southern blotting with probes 5′ and 3′ of the genomic sequence present in the targeting vector. Heterozygous *Ei24*$^{fl/wt}$ ES cell clones were microinjected into C57BL/6N blastocysts. Chimeric offspring were backcrossed to C57BL/6N mice. Heterozygous mutant mice were outbred with C57BL/6 mice and interbred to obtain homozygous mutant mice. *Cre*-mediated deletion of exon 3 leads to a frameshift, producing a small truncated peptide. The following primers were used to detect wild type *Ei24* and *Ei24*^{flox} alleles: 5′-TAAAGTTCTTAGGACACCTCCTG-3′ (*F*) and 5′-AATGGAGAACTTTAGAATCTCC-3′ (*R*). The expected sizes are 273 bp and 377 bp, respectively.

To generate neural- or liver-specific *Ei24*-deficient mice, *Ei24*$^{flox/flox}$ mice were crossed with nestin-*Cre* or albumin-*Cre* mice (Jackson Laboratory), respectively. *Ei24*$^{+/-}$ mice were obtained from *Ei24*$^{flox/wt}$; Zp3-*Cre* mice (Jackson Laboratory). All mice were raised under specific pathogen-free conditions in the animal facility at the National Institute of Biological Sciences, Beijing. All animal experiments were approved by the institutional committee of the National Institute of Biological Sciences, Beijing.

Antibodies—The following antibodies were used: rabbit anti-p62 (PM045, MBL), mouse anti-p62 (ab56416, Abcam), mouse anti-ubiquitin (3936, Cell Signaling), rabbit anti-GFAP (bs-0199R, Bioss), rabbit anti-LC3 (PM046, MBL) for Western, rabbit anti-LC3 (2775, Cell Signaling) for staining, mouse anti-NeuN (MAB377, Millipore), mouse anti-β tubulin III (ab7751, Abcam), mouse anti-calbindin (C9848, Sigma), mouse anti-CNPase (2′,3′-cyclic-nucleotide 3′-phosphodiesterase) (ab6319, Abcam), rabbit anti-MBP (myelin basic protein) (ab40390, Abcam), and rabbit anti-GFP (ab290, Abcam).

Behavioral Analysis—An accelerating rotarod (YLS-4C, Beijing Zhongshidichuang Science and Technology Development Co., Ltd) was used to measure motor coordination. After 2 consecutive days training, mice were put on the rolling rod with auto-acceleration ranging from 5–20 rpm within 60 s. The time when the mice fell from the rod was recorded, with a maximum observation time of 2 min.

Histology and Immunohistochemistry—Mice were perfused with 10% neutral buffered formalin (Sigma). Tissues were postfixed, embedded in paraffin, and sectioned at 5 μm. Sections were stained with hematoxylin and eosin for histological examination or 0.1% cresyl violet for Nissl staining and examined by light microscopy (Imager A1, Zeiss).

For immunohistochemistry, sections were deparaffinized in xylene three times, then rehydrated in an ethanol series (100% × 3, 95%, and 75%). After heat-activated antigen retrieval (0.1 M citrate buffer), sections were blocked with normal goat serum. Sections were then incubated with primary antibodies at 4 °C overnight in a humidity chamber, washed in PBS three times, and incubated with fluorescently-labeled secondary antibodies in a humidified chamber for 1 h at room temperature. Finally, sections were counterstained with DAPI, mounted and examined under an epifluorescence microscope or a confocal microscope (Zeiss LSM 510 Meta plus Zeiss Axiovert zoom). Fluorescence intensity and dot numbers were analyzed by Image J software.

Cell Counting—To score the number of spinal cord motor neurons, fixed spinal cords were sequentially sectioned at 5 μm. Every 6th section was stained with 0.1% cresyl violet. Neurons with a distinct nucleus and a diameter of at least 25 μm located in the anterior horn ventral to the line tangential to the ventral tip of the central canal were counted as motor neurons. To examine cortical neurons, large pyramidal cells located in the fifth layer of the motor and sensory cortices were quantified. The number of Purkinje cells in lobules III, IV, and V were quantified and divided by the total length of the lobules. The thickness of the molecular layer was calculated by dividing the distance between lobules III and IV, or lobules V and VI, by 2.

Protein Extraction and Western Blotting—Mouse tissues were homogenized in 10 volumes of lysis buffer (50 mM Tris-HCl, pH 7.4, 150 mM NaCl, 1 mM EDTA, 0.1% SDS, 1% Nonidet P-40) supplemented with 1 mM PMSF and protease inhibitor mixture (Roche). After incubation on ice for 30 min, homogenates were centrifuged at 15,000 rpm for 15 min at 4 °C. Supernatants were transferred to new tubes and protein concentrations were determined by Bradford protein assay (Genstar).

For preparation of detergent-soluble and -insoluble fractions, mouse tissues were homogenized in five volumes of sucrose buffer (0.25 M sucrose, 50 mM Tris-HCl, pH 7.4, and 1 mM EDTA) supplemented with 1 mM PMSF and protease inhibitors (Roche). After centrifuging at 2500 rpm for 10 min at 4 °C, the supernatants were collected, and the protein concentration was adjusted to 4 μg/μl. An aliquot of 100-μl supernatant was mixed with 100 μl of sucrose buffer containing 1% Triton X-100, then centrifuged at 15,000 rpm for 15 min at 4 °C to separate supernatants (detergent-soluble fraction) and pellets. Pellets were dissolved in 200 μl of 1% SDS in PBS (detergent-insoluble fraction). Equal amounts (30∼40 μg) of proteins were subjected to SDS-PAGE electrophoresis and then transferred onto a PVDF membrane. After blocking with 5% nonfat milk for 1 h at room temperature, membranes were incubated with primary antibodies at 4 °C overnight, washed with PBST three times and incubated with HRP-labeled secondary antibodies for 1 h at room temperature. Immunoreactivity was detected using an Enhanced Chemiluminescent (ECL) kit (Pierce).

Quantitative RT-PCR—RNA was extracted using TRIzol (Invitrogen) and cDNA was synthesized by Super Script® III First-Strand Kit (Invitrogen). Quantitative PCR was performed

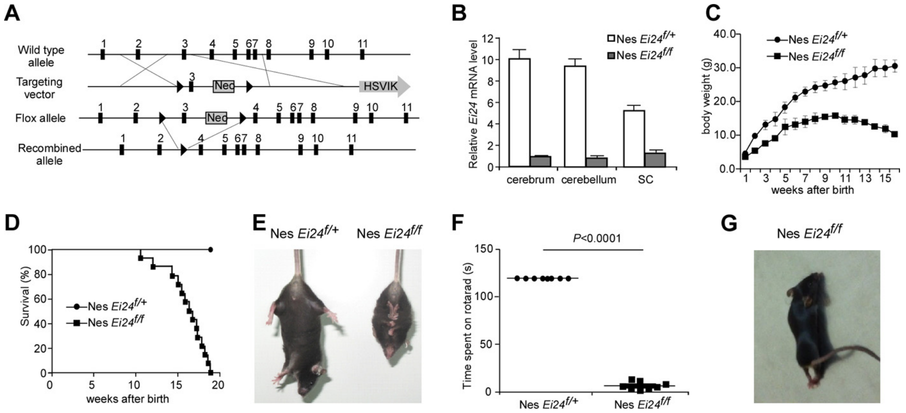

FIGURE 1. **Motor and behavioral deficits in *Ei24*$^{flox/flox}$; nestin-*Cre* mice.** *A*, scheme for generating *Ei24* conditional knock-out mice. Exons are depicted by *black boxes*. A targeting construct was prepared by flanking exon 3 of *Ei24* with the neo^r gene and loxP sites (*triangles*). The deleted allele of *Ei24* was generated by Cre-mediated recombination to remove exon 3. *B*, Nestin *Cre* effectively removes exon 3 of *Ei24* in brain tissues. Total RNAs were prepared from cerebrum, cerebellum, and spinal cord of *Ei24*$^{flox/+}$; nestin-*Cre* and *Ei24*$^{flox/flox}$; nestin-*Cre* mice at 4 months of age. Transcription levels of *Ei24* mRNA are normalized to *Actin* mRNA. Results are representative of at least three experiments. *C*, body weight curves of *Ei24*$^{flox/+}$; nestin-*Cre* and *Ei24*$^{flox/flox}$; nestin-*Cre* mice over 16 weeks. Mean ± S.E. of 18 mice is shown. *D*, survival curves of *Ei24*$^{flox/+}$; nestin-*Cre* ($n = 18$) and *Ei24*$^{flox/flox}$; nestin-*Cre* mice ($n = 18$) mice over 19 weeks. *E*, when lifted by the tail, *Ei24*$^{flox/+}$; nestin-*Cre* mice extend their limbs, while *Ei24*$^{flox/flox}$; nestin-*Cre* mice have an abnormal limb-clasping reflex, adopting a bat-like posture. *F*, time spent on an autoaccelerating rod (rotarod). The maximum observed time was 120 s. Mean ± S.E. of 9 mice is shown. *G*, when *Ei24*$^{flox/+}$; nestin-*Cre* mice initiate movement, their hindlimbs are held in a posteriorly hyperextended position.

on an Eppendorf Mastercycler® ep Realplex 4 using SYBR® Premix Ex Taq™ (TaKaRa).

The following primers were used: 5′-ACTTCCCTCTCGCTGTATTTGAT-3′ (F-*Ei24*) and 5′-TTGCTTCCGCTCTACACTCTG-3′ (R-*Ei24*); 5′-GCTGCCCTATACCCACATCT-3′ (F-*p62*) and 5′-CGCCTTCATCCGAGAAAC-3′ (R-*p62*); 5′-CTACCTTGCCCGAAAGCAC-3′ (F-*Gstm1*) and 5′-ATGTCTGCACGGATCCTCTC-3′ (R-*Gstm1*); 5′-ACCAAGGACACCAAGTTTCG-3′ (F-*Cyp2a5*) and 5′-AGAGCCCAGCATAGGAAACA-3′ (R-*Cyp2a5*); 5′-AGCGTTCGGTATTACGATCC-3′ (F-*Nqo1*) and 5′-AGTACAATCAGGGCTCTTCTCG-3′ (R-*Nqo1*); 5′-CTGGCTCCTAGCACCATGAAGAT-3′ (F-*actin*) and 5′-GGTGGACAGTGAGGCCAGGAT-3′ (R-*actin*).

Proteasome Activity Assay—Proteasome activity was determined using aminomethylcoumarin (AMC)-linked synthetic peptide substrates: Ac-Gly-Pro-Leu-Asp-AMC, Suc-Leu-Leu-Val-Tyr-AMC and Ac-Arg-Leu-Arg-AMC (and Boc-Leu-Arg-Arg-AMC) for caspase-like, chymotrypsin-like, or trypsin-like activity, respectively (Proteasome Substrate Pack, Enzo Life Sciences). Mice tissues were homogenized in lysis buffer (50 mM HEPES pH 7.5, 5 mM EDTA, 150 mM NaCl, 1% Triton X-100, and 2 mM ATP). 250 μl of lysate containing equal amounts of protein (2–4 μg) were incubated for 30 min at 37 °C in the dark with 2.5 μl of each substrate (final concentration: 50 nM). The reaction was stopped by adding 252.5 μl pre-cooled 96% ethanol solution. Proteasome activity was measured by detecting fluorescence from AMC hydrolysis (380 nm excitation and 460 nm emission).

Transmission Electron Microscopy—Mice were transcardially perfused with 2% PFA/2% glutaraldehyde buffered with 0.1 M pH 7.4 phosphate buffer (PB). Tissues were separated, fixed in 2.5% glutaraldehyde, post-fixed with 1% OsO4 in PB buffer for 2 h, dehydrated with graded ethanol solutions, and embedded in Embed812. Ultrathin sections (80 nm) were stained with 2% uranyl acetate for 30 min and lead citrate for 10 min and examined using transmission electron microscopy (Tecnai™ Spirit, FEI).

Statistical Analysis—Data from at least three sets of samples were used for statistical analysis. Statistical significance was calculated by Student's *t* test. A *p* value less than 0.05 was considered significant.

RESULTS

Neural-specific Deletion of Ei24 Causes Behavioral and Motor Abnormalities—We generated *Ei24* conditional knockout mice by flanking exon 3 of *Ei24* with two loxP sequences (Fig. 1*A*). When we crossed *Ei24*$^{+/-}$ adults (obtained from *Ei24*$^{flox/wt}$; Zp3-*Cre* mice), no *Ei24*$^{-/-}$ offspring survived to the neonatal stage, suggesting an essential role of *Ei24* during embryogenesis. The function of *Ei24* was therefore investigated by crossing *Ei24*$^{flox/flox}$ mice with mice expressing tissue-specific Cre recombinase.

Ei24$^{flox/flox}$ mice were crossed with nestin-*Cre* mice to produce animals deficient for *Ei24* in the central nervous system (referred to as *Ei24*$^{flox/flox}$; nestin-*Cre*) from embryonic stages (Fig. 1*B*). Nestin is highly expressed in neuroepithelial precursors, which give rise to neurons, astrocytes and oligodendrocytes (21). *Ei24*$^{flox/flox}$; nestin-*Cre* mice appeared normal at birth, but started to show growth retardation at 2 weeks of age and had ∼50% reduction in body weight compared with *Ei24*$^{flox/+}$; nestin-*Cre* littermates (referred to as control littermates in this study) by 3 months (Fig. 1*C*). The survival rate was also dramatically reduced; 50% of mutant mice died by ∼16 weeks after birth and all mice died by 19 weeks independent of sex (Fig. 1*D*). *Ei24*$^{flox/flox}$; nestin-*Cre* mice exhibited motor and behavioral deficits at 6 weeks of age and became progressively worse. 8 out of 12 mutant mice at 6 weeks of age and 12 out of 12 of mutant mice at 8 weeks of age exhibited abnormal limb-clasping reflexes (Fig. 1*E*). All 3-month-old mutants showed poor motor coordination in a rotarod test (Fig. 1*F*). Mutant mice exhibited marked tremor at 8 weeks and ataxic gait at 12

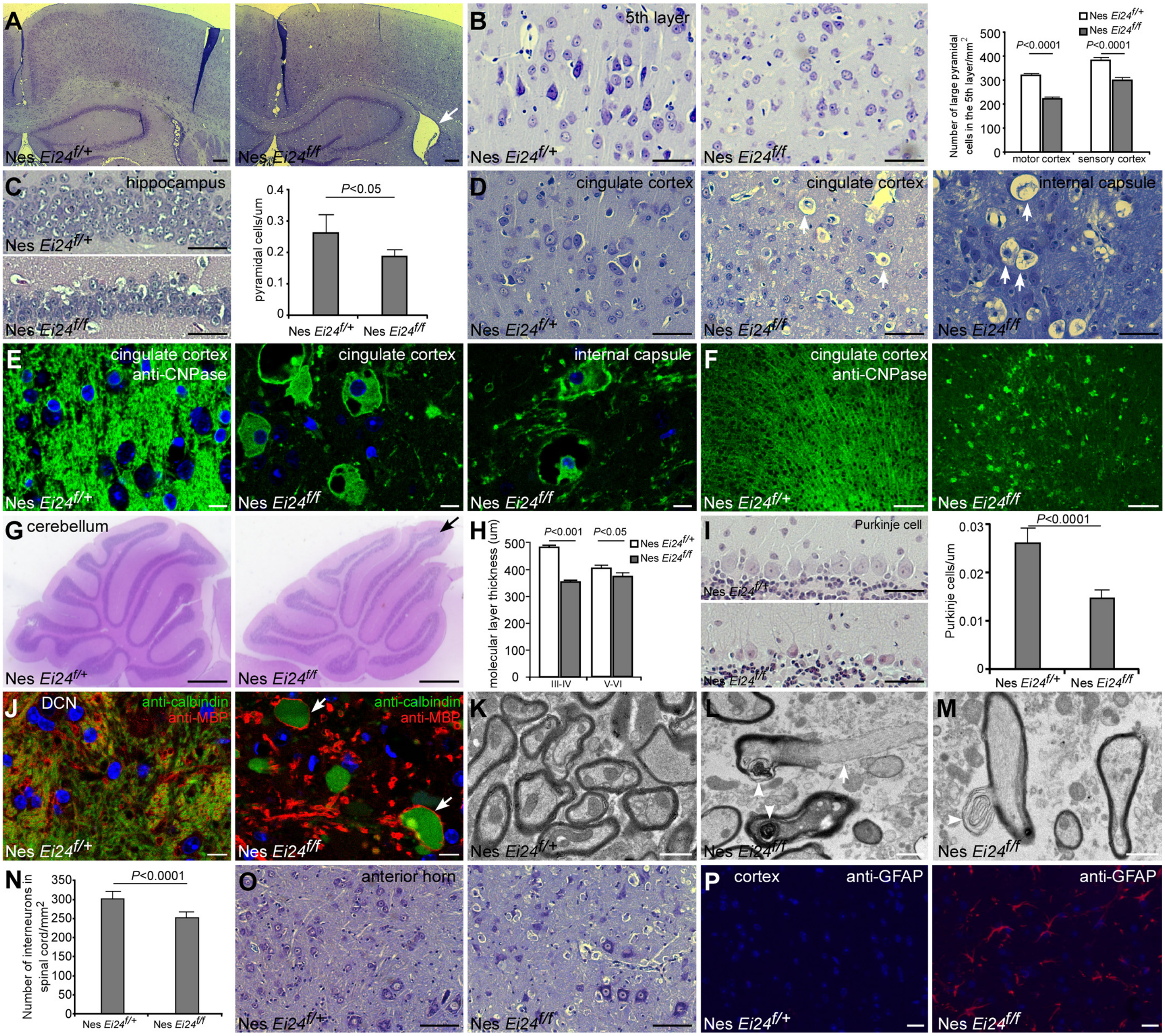

FIGURE 2. **Axonal degeneration and neuronal loss in *Ei24*$^{flox/flox}$; nestin-*Cre* mice.** *A*, Nissl staining of cortex and hippocampus of *Ei24*$^{flox/+}$; nestin-*Cre* and *Ei24*$^{flox/flox}$; nestin-*Cre* mice at 4 months of age. The *arrow* indicates an enlarged lateral ventricle. *Bar*, 200 μm. *B*, Nissl staining of the fifth layer of the cortex. The graph shows the number of large pyramidal cells per mm^2 in the indicated areas. Mean ± S.E. of three mice is shown. Bar, 50 μm. *C*, H&E staining of the hippocampal pyramidal cell layer. The number of pyramidal cells was quantified and divided by the length of the layer. Mean ± S.E. of three mice is shown. Bar, 50 μm. *D*, compared with control mice, Nissl staining of the cerebrum shows large numbers of vacuolated cells (*arrows*) in the cingulate cortex and internal capsule of *Ei24*$^{flox/flox}$; nestin-*Cre* mice. Bar, 50 μm. *E*, anti-CNPase staining show that vacuolated cells are CNPase-positive oligodendroglial cells in the cingulate cortex and internal capsule of *Ei24*$^{flox/flox}$; nestin-*Cre* mice. Bar, 10 μm. *F*, myelin stainning by anti-CNPase exhibits irregular arrangement in the cingulate cortex in *Ei24*$^{flox/flox}$; nestin-*Cre* mice at 4 months of age. Bar, 100 μm. *G*, H&E staining shows that the cerebellum is less foliated (*arrow*) and fissured in *Ei24*$^{flox/flox}$; nestin-*Cre* mice at 4 months. Bar, 500 μm. *H*, thickness of the molecular layer, calculated by dividing the distance between lobules III and IV, or lobules V and VI, by 2. Mean ± S.E. of five mice is shown. *I*, H&E staining of Purkinje cells in control and mutant mice. The number of Purkinje cells in lobules III, IV, and V was quantified and divided by the total length of the lobules. Mean ± S.E. of five mice is shown. Bar, 50 μm. *J*, anti-calbindin (*green*) and anti-MBP (*red*) costaining reveals that *Ei24*$^{flox/flox}$; nestin-*Cre* mice exhibit dilated calbindin-positive bulbs (*arrows*) in the DCN region and some of the bulbs are enwrapped by MBP-labeled myelin. Bar, 10 μm. *K–M*, EM pictures of DCN in *Ei24*$^{flox/+}$; nestin-*Cre* and *Ei24*$^{flox/flox}$; nestin-*Cre* mice at 4 months. *K*, myelinated axons of regular shape and size in the DCN region of control animals. (*L–M*), Degenerated axons in mutant mice. *L*, *arrowheads* indicate electron-dense amorphous structures. The *arrow* shows a thinned myelin sheath. *M*, *arrowhead* indicates undulated and split myelin lamellae. Note that the axons in the mutant sample are conspicuously less abundant than in the control. Bar, 1 μm (*K–M*). *N*, number of interneurons per mm^2 in the lumbar spinal cord. Mean ± S.E. of five mice is shown. *O*, accumulation of vacuolated cells in the anterior horn of the lumbar spinal cord in mutant mice at 4 months. Bar, 100 μm. *P*, GFAP signal (*red*), in sections of cerebral cortex immunostained with anti-GFAP antibody, is stronger in mutant mice. Bar, 20 μm.

weeks. At 14 weeks, the hindlimbs of resting mutant mice were flexed, like control littermates, but became hyperextended posteriorly during movement (Fig. 1*G*; supplemental movie). Thus, neural-specific *Ei24* deficiency causes behavioral and motor defects.

Ei24$^{flox/flox}$; nestin-Cre Mice Suffer Massive Axonal Degeneration and Neuronal Cell Loss—To investigate the neural defect in *Ei24*$^{flox/flox}$; nestin-*Cre* mice, histological analyses were performed by hematoxylin and eosin (H&E) staining and Nissl staining of sections from cerebrum, cerebellum, and spinal cord

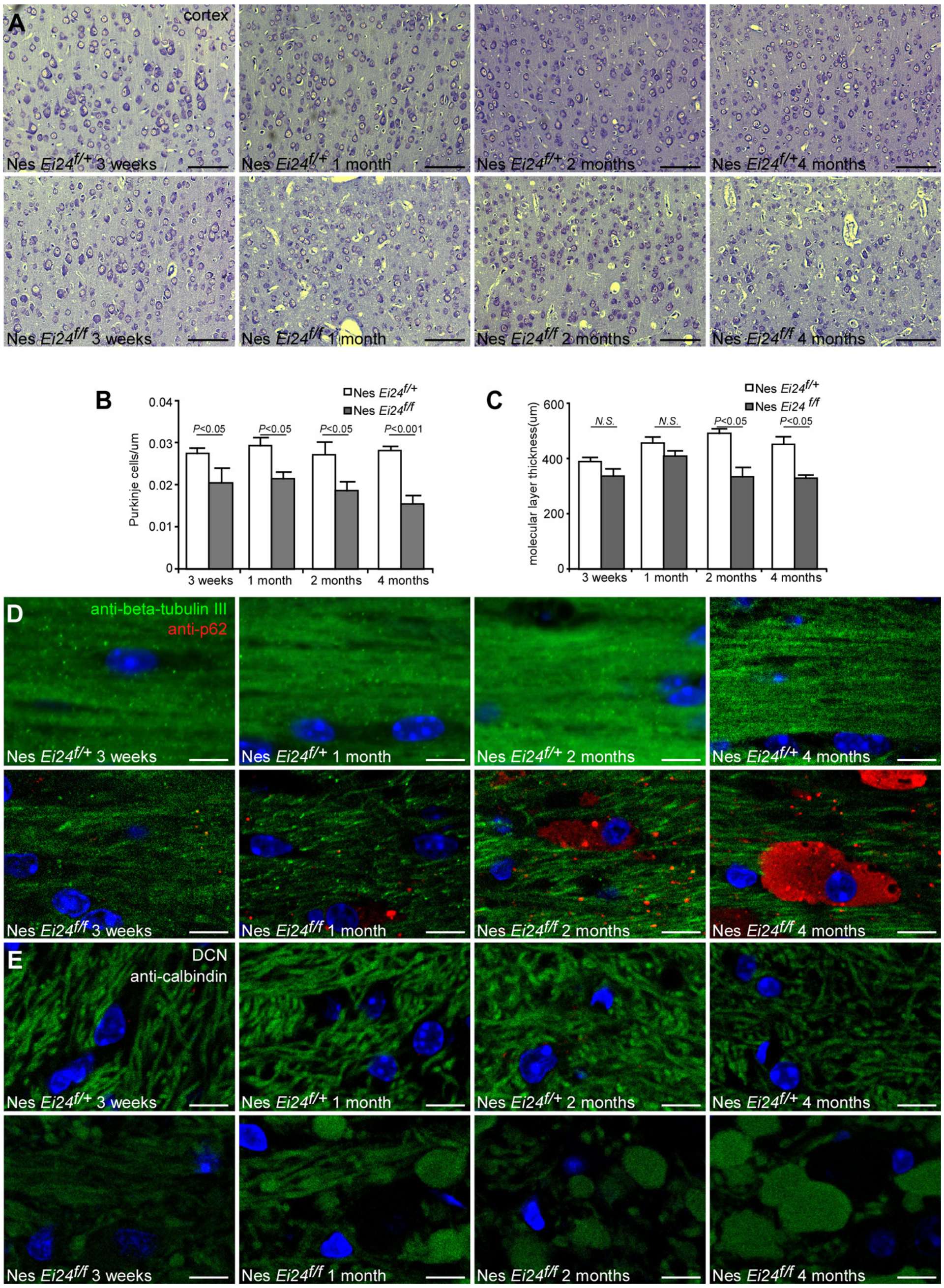

FIGURE 3. **Progressive deterioration in cerebrum, cerebellum and spinal cord of *Ei24*$^{flox/flox}$; nestin-*Cre* mice.** *A*, Nissl staining of the cortex in control and *Ei24*$^{flox/flox}$; nestin-*Cre* mice at different ages shows progressive accumulation of vacuolated cells. Bar, 100 μm. *B* and *C*, number of Purkinje cells (*B*) and the thickness of the molecular layer (*C*) in cerebella from *Ei24*$^{flox/flox}$; nestin-*Cre* mice at different ages. *D*, costaining of β-tubulin III (*green*) and p62 (*red*) in cerebrum shows that axonal fibers become progressively more irregularly arranged. p62 aggregates and diffuse levels of p62 in *Ei24*$^{flox/flox}$; nestin-*Cre* also become dramatically elevated with age. Bar, 10 μm. *E*, axon terminals of Purkinje cells in the DCN region, stained by anti-calbindin, become progressively more dilated. Bar, 10 μm.

of control and mutant mice at 4 months of age. *Ei24*$^{flox/flox}$; nestin-*Cre* brains had enlarged lateral ventricles (Fig. 2*A*). Mutant mice showed atrophy of the cerebral cortex (Fig. 2*A*); the ratio of cortical to dorsoventral thickness in *Ei24*$^{flox/+}$; nestin-*Cre* and *Ei24*$^{flox/flox}$; nestin-*Cre* mice was 0.18 ± 0.02 and 0.13 ± 0.01, respectively ($p < 0.05$). The white matter between the cortex and hippocampal pyramidal cells was thinner in mutants (Fig. 2*A*). The number of neurons in cortical layers 1–4 was greatly reduced compared with controls, as was the number of pyramidal neurons in the 5th layer of the motor and sensory cortices (Fig. 2*B*; supplemental Fig. S1, *B* and *C*). The hippocampal pyramidal cell layer was much thinner with reduced neuron numbers (Fig. 2*C*). H&E and axon-specific β-tubulin III staining revealed irregularly arranged nerve fibers in the alveus of the hippocampus (supplemental Fig. S1, *D* and *E*). Eosinophilic spheroids, representing axon swellings (10), were observed in the cortex (supplemental Fig. S1*F*). Vacuolated cells were observed in the cingulate cortex and to a lesser extent in other cortices, hippocampus, thalamus, and hypothalamus (Fig. 2*D*). Numerous vacuolated cells were found in white

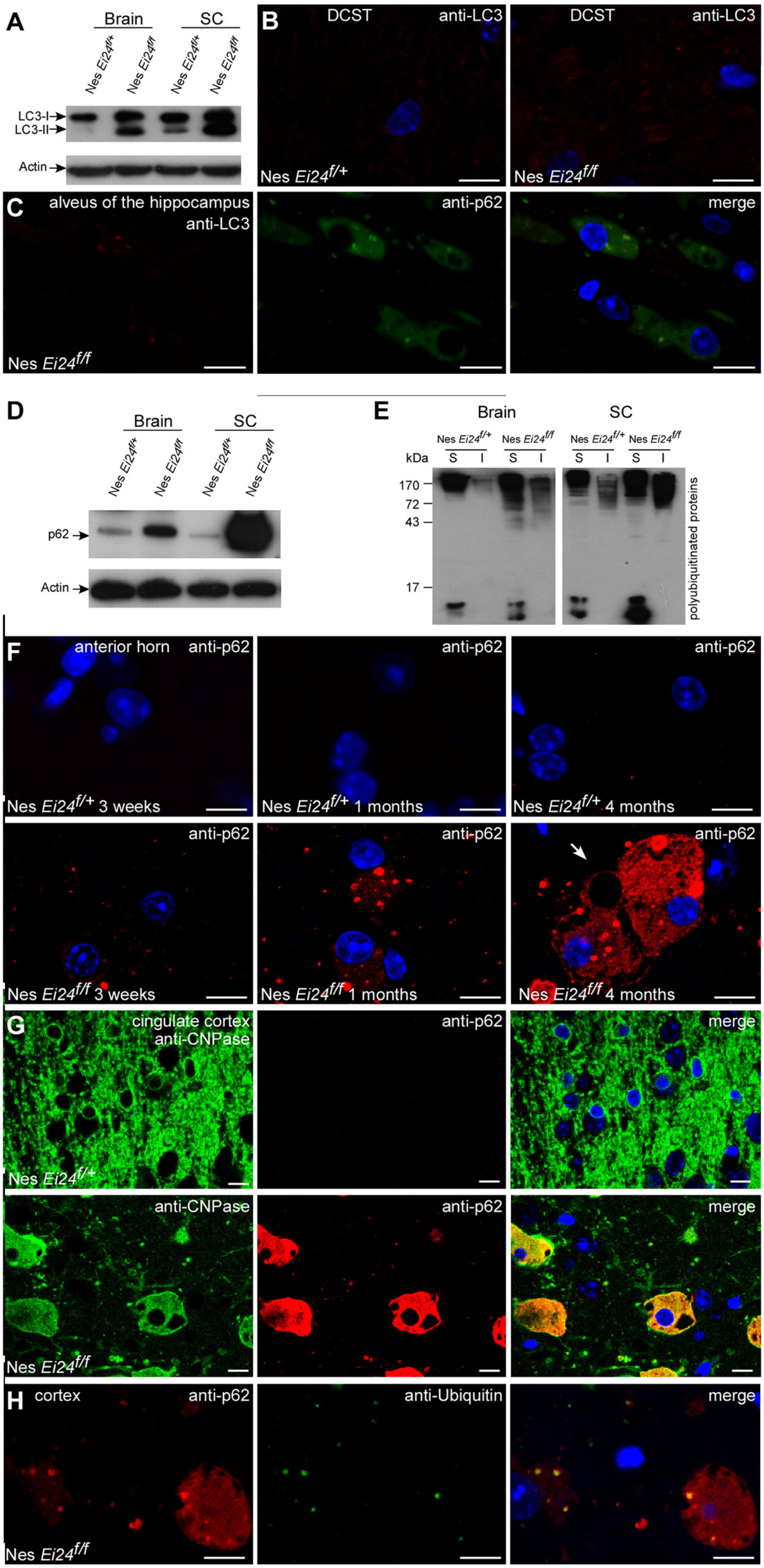
A
Brain
SC
Nes Ei24f/+
Nes Ei24f/f
Nes Ei24f/+
Nes Ei24f/f
LC3-I
LC3-II
Actin
B
DCST
anti-LC3
DCST
anti-LC3
Nes Ei24f/+
Nes Ei24f/f
C
alveus of the hippocampus
anti-LC3
anti-p62
merge
Nes Ei24f/f
D
Brain
SC
Nes Ei24f/+
Nes Ei24f/f
Nes Ei24f/+
Nes Ei24f/f
p62
Actin
E
Brain
SC
Nes Ei24f/+
Nes Ei24f/f
Nes Ei24f/+
Nes Ei24f/f
kDa
S
I
S
I
S
I
S
I
170
72
43
17
polyubiquitinated proteins
F
anterior horn
anti-p62
anti-p62
anti-p62
Nes Ei24f/+ 3 weeks
Nes Ei24f/+ 1 months
Nes Ei24f/+ 4 months
anti-p62
anti-p62
anti-p62
Nes Ei24f/f 3 weeks
Nes Ei24f/f 1 months
Nes Ei24f/f 4 months
G
cingulate cortex
anti-CNPase
anti-p62
merge
Nes Ei24f/+
anti-CNPase
anti-p62
merge
Nes Ei24f/f
H
cortex
anti-p62
anti-Ubiquitin
merge
Nes Ei24f/f

matter regions including the corpus callosum, the alveus of the hippocampus and the internal capsule (Fig. 2*D*, supplemental Fig. S1*D*, data not shown). The vacuolated cells were stained by the oligodendroglial marker anti-2′,3′-cyclic-nucleotide 3′-phosphodiesterase (CNPase) (Fig. 2*E*). Oligodendrocytes support axonal integrity and myelinate the axons of the CNS (22). Staining with anti-myelin basic protein (MBP) (which labels myelin) or anti-CNPase (which labels cell bodies and myelin) revealed fragmented myelin structures in various cerebral regions in mutant mice (Fig. 2*F*; supplemental Fig. S1*G*).

The cerebella of *Ei24$^{flox/flox}$*; nestin-*Cre* mice were less foliated and fissured than controls (Fig. 2*G*). The molecular cell layer was thinner (Fig. 2*H*). Purkinje cell numbers were reduced by 40% and the remaining cells appeared shrunken (Fig. 2*I*). The deep cerebellar nuclei (DCN), to which Purkinje cells project axons, contained numerous large eosinophilic spheroid structures (supplemental Fig. S1*H*), indicative of axonal swellings (10). We further stained the DCN region with anti-calbindin, which specifically labels Purkinje axons, and found accumulation of huge bulging calbindin-positive structures in the DCN region of *Ei24$^{flox/flox}$*; nestin-*Cre* mice, indicating abnormal swelling and dystrophy of Purkinje cell axon terminals (Fig. 2*J*). MBP staining showed that some of the dilated calbindin-positive termini were enwrapped by myelin, confirming the degeneration of Purkinje cell axons (Fig. 2*J*; supplemental Fig. S1, *I–J*). Ultrastructurally, axon numbers in the DCN region were dramatically reduced and the remaining axons showed thinned, split myelin sheaths and various signs of degeneration (Fig. 2, *K--M*; supplemental Fig. S1, *K–N*). In the anterior horn of the lumbar spinal cord, interneuron numbers were dramatically reduced in *Ei24$^{flox/flox}$*; nestin-*Cre* mice but the number of large motor neurons was not significantly different (Fig. 2*N*; supplemental Fig. S1, *O* and *P*). Numerous vacuolated oligodendrocytes accumulated in spinal cord gray and white matter (Fig. 2*O*; supplemental Fig. S1*Q*). Expression of the glial marker GFAP (glial fibrillary acidic protein) dramatically increased in the cerebrum, cerebellum and spinal cord of mutant mice (Fig. 2*P*), indicating that neurodegeneration was accompanied by reactive astrogliosis.

To investigate whether the neural abnormalities in *Ei24$^{flox/flox}$*; nestin-*Cre* mice increase progressively, brain and spinal cord sections from *Ei24$^{flox/flox}$*; nestin-*Cre* mice and controls at 3 weeks, one month, two months, and four months were analyzed. The number of pyramidal neurons in the 5th layer of the cortex in *Ei24$^{flox/flox}$*; nestin-*Cre* mice at 3 weeks of age was comparable to control littermates, but gradually decreased as the mice grew older (Fig. 3*A*). The number of Purkinje cells and thickness of the molecular layer progressively decreased (Fig. 3, *B* and *C*). Vacuolated oligodendrocytes in the cerebrum, cerebellum, and spinal cord were small in size and few in number in mutant mice at 3 weeks and one month of age but became larger and more numerous at 2 and 4 months of age (Fig. 3*A*; supplemental Fig. S2, *A* and *B*). The mutant mice also showed progressively more irregularly arranged nerve fibers in the alveus of the hippocampus, more severe axonal swelling in the DCN of the cerebellum and deterioration of axonal myelin sheaths in various regions of the brain and spinal cord (Fig. 3, *D* and *E*; supplemental Fig. 2*C*). Thus, neural-specific *Ei24* deficiency results in progressive axonal degeneration and neuronal loss.

Ei24 Deficiency Impairs Autophagic Flux—We next investigated autophagic flux in mutant mice by examining levels and distribution of LC3. Brain and spinal cord extracts from *Ei24$^{flox/flox}$*; nestin-*Cre* mice at 4 months showed accumulation of LC3-II, a lipidated form of LC3 that normally associates with autophagosomal membranes (Fig. 4*A*). Immunostaining with anti-LC3 revealed that LC3 diffusely accumulated in various regions of the brain and spinal cord of *Ei24$^{flox/flox}$*; nestin-*Cre* mice at 4 months (Fig. 4*B*; supplemental Fig. S3, *A–C*). LC3 puncta were largely absent, apart from a few that accumulated in white matter regions, such as the alveus of hippocampus in the cerebrum, DCN in cerebellum and the LC (lateral column) in spinal cord (Fig. 4*C*; supplemental Fig. S3, *A*, *B*, *D*).

Accumulation of p62 and ubiquitinated protein aggregates is one of the hallmarks of autophagy deficiency (23). p62 is required for formation and selective removal of ubiquitin-positive aggregates (12). Brain and spinal cord extracts from mutant mice at 4 months showed dramatic accumulation of p62 and high-molecular mass polyubiquitinated proteins (Fig. 4, *D* and *E*). *p62* mRNA levels were not up-regulated in mutants (supplemental Fig. S3*E*). Polyubiquitinated proteins showed age-dependent progressive accumulation in *Ei24$^{flox/flox}$*; nestin-*Cre* mice (supplemental Fig. S3*F*). Impaired proteasome function can also cause accumulation of p62 and polyubiquitinated proteins; however, proteasomal caspase-like, chymotryptic, and tryptic activities, measured using specific substrate peptides, were comparable in controls and mutants (supplemental Fig. S3*G*).

We next examined the distribution of p62 and ubiquitinated proteins in mutant mice. Control brain and spinal cord contained very little or no cytoplasmic p62 and ubiquitin-positive aggregates (Fig. 4*F*; supplemental Fig. S3, *H* and *K*). In 3-week-old *Ei24$^{flox/flox}$*; nestin-*Cre* mice, the cerebrum, cerebellum and spinal cord accumulated numerous small p62 aggregates, which increased in size and number with age (Fig. 4*F*). p62

FIGURE 4. **Accumulation of LC3-II, p62 aggregates and ubiquitin-positive inclusions in neural-deficient *Ei24* mice.** *A*, total brain and spinal cord proteins from *Ei24$^{flox/+}$*; nestin-*Cre* and *Ei24$^{flox/flox}$*; nestin-*Cre* mice at 4 months of age were extracted and separated by SDS-PAGE and analyzed by immunoblotting with anti-LC3 antibodies. Results are representative of at least three experiments. *B*, anti-LC3 (*red*) staining reveals that *Ei24$^{flox/flox}$*; nestin-*Cre* mice exhibit stronger diffuse LC3 signal in the DCST (dorsal corticospinal tract) of spinal cord. Bar, 10 μm. *C*, a few LC3 puncta colocalize with p62 aggregates in the the alveus of the hippocampus of *Ei24$^{flox/flox}$*; nestin-*Cre* mice at 4 months. Bar, 10 μm. *D*, *Ei24$^{flox/flox}$*; nestin-*Cre* mice at 4 months of age show p62 accumulation in brain and spinal cord by immunoblotting with p62 antibodies. Results are representative of at least three experiments. *E*, immunoblotting assay showing polyubiquitinated proteins in detergent-soluble and detergent-insoluble fractions of brain and spinal cord (*SC*) homogenates from control and mutant mice. Results are representative of at least three experiments. *F*, p62 aggregates are absent from the anterior horn of the spinal cord of *Ei24$^{flox/+}$*; nestin-*Cre* mice. p62 aggregates (*red*) progressively accumulate in mutant mice at 3 weeks, 1 month, and 4 months of age. Levels of diffuse p62 are also elevated especially in vacuolated cells (*arrow*). Bar, 10 μm. *G*, anti-CNPase and anti-p62 costaining show that compared with controls diffuse p62 and the majority of p62 aggregates are located in CNPase-positive oligodendroglial cells in the cingulate cortex of *Ei24$^{flox/flox}$*; nestin-*Cre* mice. Bar, 10 μm. *H*, compared with control animals, p62 (*red*) and ubiquitinated proteins (*green*) accumulate and are colocalized in cerebrum sections of *Ei24$^{flox/flox}$*; nestin-*Cre* mice. p62 aggregates are more numerous than ubiquitinated protein inclusions. Bar, 10 μm.

accumulated most heavily in the alveus of the hippocampus and the internal capsule, where vacuolated oligodendrocytes were present. p62 aggregates mainly accumulated in oligodendrocytes (identified with CNPase) and were also detected in neurons (identified with NeuN) (Fig. 4*G*; supplemental Fig. S3, *H* and *I*), but were hardly observed in GFAP-labeled astroglia or

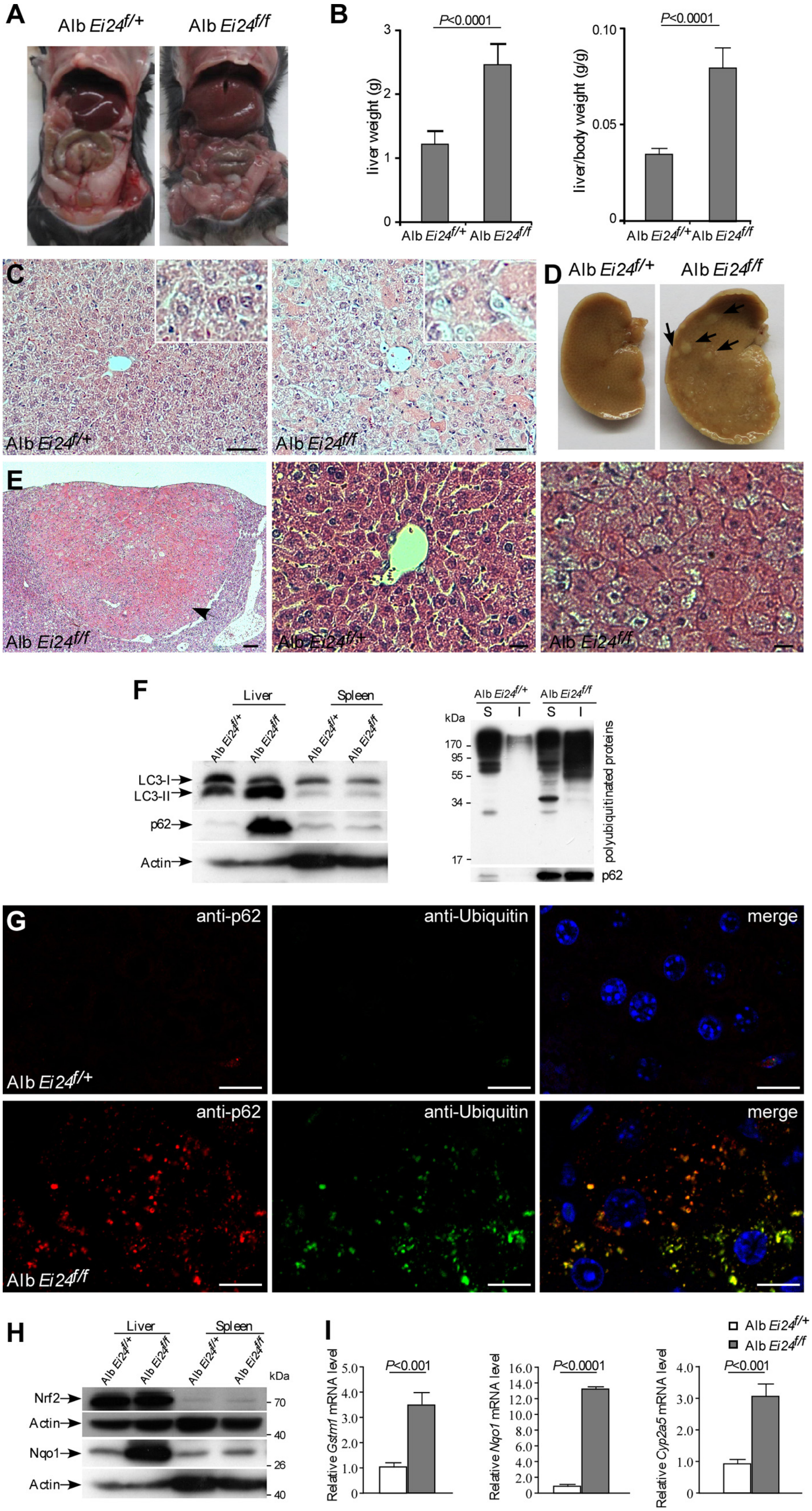

calbindin-stained axonal swellings (supplemental Fig. S3, *J–L*). The level of diffuse cytoplasmic p62 was also greatly elevated in mutant mice, especially in vacuolated oligodendrocytes (Fig. 4, *C*, *F*, *G*). Ubiquitin-positive aggregates colocalized with p62 aggregates in *Ei24*$^{flox/flox}$; nestin-*Cre* mice, but they were fewer in number than p62 aggregates (Fig. 4*H*). The few LC3 puncta were colocalized with p62 aggregates (Fig. 4*C*; supplemental Fig. S3*B*). Thus, autophagy is defective in neural-specific *Ei24*-deficient mice.

Liver-specific Depletion of Ei24 Causes Hepatomegaly and Multiple Tumor-like Protrusions—Ei24$^{flox/flox}$ mice were crossed with mice expressing *Cre* controlled by the albumin promoter to deplete *Ei24* in the liver (supplemental Fig. S4*A*). *Ei24*$^{flox/flox}$; Alb-*Cre* mice appeared normal at birth but by 3 months their livers were greatly enlarged, with disorganized hepatic lobules and swollen appearance of hepatocytes that were mixed with normal appearance hepatocytes (Fig. 5, *A–C*). Unlike *Ei24*-deficient neuronal cells, vacuolization of hepatocytes was not obvious in *Ei24*$^{flox/flox}$; Alb-*Cre* livers at 3 months. Ultrastructurally, swollen mitochondria accumulated in mutant hepatocytes (supplemental Fig. S4*C*). Activities of alkaline phosphatase and aspartate aminotransferase were significantly elevated in mutant mice sera, suggesting hepatic cell death (supplemental Fig. S4*D*). By 10 months, multiple tumor-like protrusions were detected in mutant livers (Fig. 5*D*). Histological analyses revealed that these protrusions were composed of enlarged hepatocytes and were demarcated from neighboring hepatocytes of normal size (Fig. 5*E*). However, no signs of malignancy such as abnormal nuclear morphology were detected in the protrusions.

We examined autophagic flux and found that liver homogenates from *Ei24*$^{flox/flox}$; Alb-*Cre* mice at 3 months contained dramatically elevated LC3-II, p62, and polyubiquitinated proteins (Fig. 5*F*). p62 aggregates and ubiquitin-positive inclusions accumulated and colocalized in swollen hepatocytes (Fig. 5*G*; supplemental Fig. S4, *E* and *F*). Diffuse p62 was much weaker than in *Ei24*-deficient neural cells. LC3 formed a few puncta that colocalized with p62 aggregates in mutant liver at 3 months (supplemental Fig. S4, *G* and *H*).

Ei24 Deficiency Activates the Nrf2-mediated Stress Response Pathway in Liver—Dramatic accumulation of p62 aggregates in *Ei24*-deficient liver prompted us to examine whether the Nrf2 stress response is activated. p62 accumulation causes sequestration of Keap1, a component of the Cullin-3-type ubiquitin ligase for Nrf2 degradation, and subsequently leads to stabilization of Nrf2 and transcriptional activation of Nrf2 target genes including those encoding various anti-oxidant and detoxifying enzymes (24). *Ei24* deletion caused no changes in levels of Nrf2 (Fig. 5*H*). Immunoblotting showed that levels of the Nrf2 target NAD(P)H dehydrogenase quinone 1 (Nqo1) were elevated in the liver of *Ei24*$^{flox/flox}$; Alb-*Cre* mice at 3 months of age (Fig. 5*H*). Quantitative RT-PCR showed dramatically elevated mRNA levels of *Gstm1* (glutathione *S*-transferase), *Nqo1*, and *Cyp2a5* (cytochrome 450), but not *p62*, in mutant liver (Fig. 5*I*, supplemental Fig. S4*I*). These detoxifying enzyme genes, however, were not up-regulated in the brains of *Ei24*$^{flox/+}$; nestin-*Cre* mice (supplemental Fig. S4*J*), suggesting that persistent Nrf2 activation may be tissue specific.

DISCUSSION

Here we demonstrated that mice deficient for the metazoan-specific autophagy gene *Ei24* show degeneration of neuronal populations and severe liver injury. The behavioral and motor abnormalities in mice with neural-specific *Ei24* depletion are similar to, but more severe than, those in *Atg5* and *Atg7* conditional knock-out mice. All *Ei24*-deficient mice die before 19 weeks, while *Atg7*-deficient mice reach 28 weeks (11). *Ei24* deficiency results in massive vacuolated oligodendrocytes that are not observed in *Atg5* and *Atg7* knock-out mice (10–12). Oligodendrocytes support axonal integrity and myelinate axons for rapid impulse propagation in the CNS, and their dysfunction, as seen in *Cnp1* knock-out mice, causes axonal swelling and neurodegeneration throughout the brain (22, 25). Accumulation of p62 aggregates and ubiquitin-positive inclusions in *Ei24*-deficient tissues indicates that in addition to neurons, autophagy plays an important role in homeostatic maintenance of oligodendroglial cells. EI24 is an ER-localized protein and may have functions independent of autophagy, which could explain why oligodendrocytes are more severely impaired in *Ei24*-deficient mice than in other autophagy knockouts. *Atg5* and *Atg7* deficiency cause intrinsic cell-autonomous neuronal cell death (26, 27). Compared with *Atg5* and *Atg7* knock-out mice, *Ei24*-deficient mice exhibit less severe accumulation of p62 and ubiquitin-positive aggregates in neurons, which could be because the axonal degeneration and neuronal loss in *Ei24* mutants are severely exacerbated by the more pronounced dysfunction of vacuolated oligodendrocytes. The pathological defects associated with *Ei24* deficiency are cell-type specific. *Ei24*-deficient liver exhibits similar defects to *Atg5*- and *Atg7*-deficient liver, including hepatocyte hypertrophy, hepatic cell death and hepatomegaly (13, 14). However, the tumor-like protrusions in *Ei24*-deficient liver are composed of enlarged hepatocytes and

FIGURE 5. **Liver-specific deletion of *Ei24* causes hepatomegaly and autophagy defects.** *A*, gross anatomical views of representative livers from *Ei24*$^{flox/+}$; Alb-*Cre* and *Ei24*$^{flox/flox}$; Alb-*Cre* mice at 3 months of age. Livers in *Ei24*$^{flox/flox}$; Alb-*Cre* mice are enlarged. *B*, graphs showing net weight of livers and ratio of liver/body weight in control and mutant mice. Mean ± S.E. of 3 mice is shown. *C*, H&E-stained liver sections from control and mutant mice show disorganized hepatic lobules and swollen hepatocytes in *Ei24*$^{flox/flox}$; Alb-*Cre* mice. *Insets* show higher magnification views. Bar, 50 μm. *D*, gross anatomy of livers from *Ei24*$^{flox/flox}$; Alb-*Cre* mice at 10 months of age demonstrates the development of multiple tumor-like protrusions (*arrows*). *E*, H&E staining of liver sections from *Ei24*$^{flox/flox}$; Alb-*Cre* mice at 10 months of age (*first panel*). The *arrow* indicates a tumor-like protrusion. Bar, 100 μm. Higher magnification images of livers from controls (*second panel*) and *Ei24*-deficient mice (*third panel*, protrusion region) at 10 months of age. Bar, 20 μm. *F*, accumulation of LC3-II, p62 and polyubiquitinated proteins in livers from *Ei24*$^{flox/flox}$; Alb-*Cre* mice. Total liver and spleen proteins were extracted, separated by SDS-PAGE, and analyzed by immunoblotting with anti-LC3 and anti-p62 antibodies. Detergent-soluble and detergent-insoluble fractions from liver homogenates were immunoblotted with anti-ubiquitin and anti-p62 antibodies. *G*, coimmunostaining with anti-p62 (*red*) and anti-ubiquitin (*green*) antibodies reveals that p62 and ubiquitin-positive aggregates are absent from control liver sections, but accumulate heavily in liver sections of *Ei24*$^{flox/flox}$; Alb-*Cre* mice. p62 aggregates colocalize with ubiquitin-positive inclusions in mutant liver. Bar, 10 μm. *H*, immunoblotting with anti-Nqo1 antibody shows that the Nqo1 protein level is dramatically elevated in *Ei24*$^{flox/flox}$; Alb-*Cre* mice. Levels of Nrf2 remain unchanged in control and *Ei24*-deficient liver. *I*, *Gstm1*, *Nqo1*, and *Cyp2a5* mRNA levels are increased in *Ei24*-deficient mice. The *Gstm1*, *Nqo1*, and *Cyp2a5* transcription levels were normalized to actin mRNA. Results are representative of at least three experiments.

display no signs of malignancy. These protrusions could be caused by aggregation of abnormal enlarged hepatocytes. Reduced *Ei24* expression in aggressive breast cancers implicates it is a tumor suppressor (3, 5). Autophagy suppresses tumorigenesis through suppression of tumorigenic inflammation, surveillance of genome stability and elimination of p62 (14–16). The essential role of *Ei24* in autophagy may contribute to its tumor suppression function in other tissues. Distinct defects in *Ei24*-deficient liver and brain could be caused by tissue-specific activation of Nrf2 by p62 accumulation. Antioxidant and detoxifying enzymes, including *Nqo1*, *Gstm1*, and *Cyp2a5*, are highly expressed in *Ei24*-deficient liver, but not in the brains of *Ei24*-deficient mice. Simultaneous depletion of *p62* or *Nrf2* significantly suppresses liver injury in *Atg7*-deficient mice, including increased liver weight, disorganization of lobular structures and hepatocyte hypertrophy (12, 24). However, ablation of p62 does not suppress neurodegeneration caused by autophagy deficiency (12).

The molecular role of *Ei24* in the autophagy pathway has yet to be determined. EI24/EPG-4 is an ER-localized protein with six transmembrane domains. PI(3)P-enriched ER subdomains, known as omegasomes, are known to be the membrane source for autophagosome formation (18). Several ATG proteins involved in early steps of autophagy, including ULK1 and ATG14, tightly associate with the ER, and are required for formation of LC3 puncta (autophagosomes) (28). Consistent with a role in early autophagy, EPG-4 regulates the progression of omegasomes to autophagosomes (20). However, knockdown of *Ei24* appears to cause a defect in the degradation step of the autophagy pathway. Enlarged nondegradative autolysosomes accumulate in *Ei24* siRNA knockdown cells (20). In *Ei24*-deficient mice, lipidated LC3 accumulates dramatically and is diffusely localized, suggesting that *Ei24* acts at an early step of autophagosome formation. The few LC3 puncta detected in *Ei24*-deficient mice are likely due to incorporation of LC3 into p62 aggregates via direct p62/LC3 interaction. Alternatively, p62 aggregates may accumulate in impaired autolysosomes due to a defect in the degradation step of the autophagy pathway. *Ei24* is highly induced by p53 in various cell types. p53 induces autophagy activity by inhibiting mTOR activity and also by up-regulating the lysosomal protein DRAM (29, 30). Distinct from *Atg* genes and *Ei24*, DRAM is critical for induction of autophagy in the specific context of p53 activation and is not required for basal autophagy (30). The essential role of *Ei24* in basal autophagy indicates that p53 may regulate autophagy activity by integrating with the core autophagic machinery.

Acknowledgments—We thank Drs. Zelda Cheung, Masaaki Komatsu, and Waguri Satoshi for helpful comments on the manuscript and Dr. Isabel Hanson for editing work.

REFERENCES

1. Lehar, S. M., Nacht, M., Jacks, T., Vater, C. A., Chittenden, T., and Guild, B. C. (1996) Identification and cloning of EI24, a gene induced by p53 in etoposide-treated cells. *Oncogene* **12,** 1181–1187
2. Gu, Z., Flemington, C., Chittenden, T., and Zambetti, G. P. (2000) ei24, a p53 response gene involved in growth suppression and apoptosis. *Mol. Cell. Biol.* **20,** 233–241
3. Zhao, X., Ayer, R. E., Davis, S. L., Ames, S. J., Florence, B., Torchinsky, C., Liou, J. S., Shen, L., and Spanjaard, R. A. (2005) Apoptosis factor EI24/PIG8 is a novel endoplasmic reticulum-localized Bcl-2-binding protein which is associated with suppression of breast cancer invasiveness. *Cancer Res.* **65,** 2125–2129
4. Mork, C. N., Faller, D. V., and Spanjaard, R. A. (2007) Loss of putative tumor suppressor EI24/PIG8 confers resistance to etoposide. *FEBS Letters* **2581,** 5440–5444
5. Gentile, M., Ahnström, M., Schön, F., and Wingren, S. (2001) Candidate tumour suppressor genes at 11q23-q24 in breast cancer: evidence of alterations in PIG8, a gene involved in p53-induced apoptosis. *Oncogene* **20,** 7753–7760
6. Xie, Z., and Klionsky, D. J. (2007) Autophagosome formation: core machinery and adaptations. *Nat. Cell Biol.* **9,** 1102–1109
7. Nakatogawa, H., Suzuki, K., Kamada, Y., and Ohsumi, Y. (2009) Dynamics and diversity in autophagy mechanisms: lessons from yeast. *Nat. Rev. Mol. Cell Biol.* **10,** 458–467
8. Levine, B., and Kroemer, G. (2008) Autophagy in the pathogenesis of disease. *Cell* **132,** 27–42
9. Ichimura, Y., and Komatsu, M. (2011) Pathophysiological role of autophagy: lesson from autophagy-deficient mouse models. *Exp. Anim.* **60,** 329–345
10. Hara, T., Nakamura, K., Matsui, M., Yamamoto, A., Nakahara, Y., Suzuki-Migishima, R., Yokoyama, M., Mishima, K., Saito, I., Okano, H., and Mizushima, N. (2006) Suppression of basal autophagy in neural cells causes neurodegenerative disease in mice. *Nature* **441,** 885–889
11. Komatsu, M., Waguri, S., Chiba, T., Murata, S., Iwata, J., Tanida, I., Ueno, T., Koike, M., Uchiyama, Y., Kominami, E., and Tanaka, K. (2006) Loss of autophagy in the central nervous system causes neurodegeneration in mice. *Nature* **441,** 880–884
12. Komatsu, M., Waguri, S., Koike, M., Sou, Y. S., Ueno, T., Hara, T., Mizushima, N., Iwata, J., Ezaki, J., Murata, S., Hamazaki, J., Nishito, Y., Iemura, S., Natsume, T., Yanagawa, T., Uwayama, J., Warabi, E., Yoshida, H., Ishii, T., Kobayashi, A., Yamamoto, M., Yue, Z., Uchiyama, Y., Kominami, E., and Tanaka, K. *(*2007) Homeostatic levels of p62 control cytoplasmic inclusion body formation in autophagy-deficient mice. *Cell* **131,** 1149–1163
13. Komatsu, M., Waguri, S., Ueno, T., Iwata, J., Murata, S., Tanida, I., Ezaki, J., Mizushima, N., Ohsumi, Y., Uchiyama, Y., Kominami, E., Tanaka, K., and Chiba, T. *(*2005) Impairment of starvation-induced and constitutive autophagy in Atg7-deficient mice. *J. Cell Biol.* **169,** 425–434
14. Takamura, A., Komatsu, M., Hara, T., Sakamoto, A., Kishi, C., Waguri, S., Eishi, Y., Hino, O., Tanaka, K., and Mizushima, N. (2011) Autophagy-deficient mice develop multiple liver tumors. *Genes Dev.* **25,** 795–800
15. Mathew, R., Karp, C. M., Beaudoin, B., Vuong, N., Chen, G., Chen, H. Y., Bray, K., Reddy, A., Bhanot, G., Gelinas, C., Dipaola, R. S., Karantza-Wadsworth, V., and White, E. (2009) Autophagy suppresses tumorigenesis through elimination of p62. *Cell* **137,** 1062–1075
16. Inami, Y., Waguri, S., Sakamoto, A., Kouno, T., Nakada, K., Hino, O., Watanabe, S., Ando, J., Iwadate, M., Yamamoto, M., Lee, M. S., Tanaka, K., and Komatsu, M. (2011) Persistent activation of Nrf2 through p62 in hepatocellular carcinoma cells. *J. Cell Biol.* **193,** 275–284
17. Longatti, A., and Tooze, S. A. (2009) Vesicular trafficking and autophagosome formation. *Cell Death Differ.* **16,** 956–965
18. Tooze, S. A., and Yoshimori, T. (2010) The origin of the autophagosomal membrane. *Nat. Cell Biol.* **12,** 831–835
19. Ravikumar, B., Moreau, K., Jahreiss, L., Puri, C., and Rubinsztein, D. C. (2010) Plasma membrane contributes to the formation of pre-autophagosomal structures. *Nat. Cell Biol.* **12,** 747–757
20. Tian, Y., Li, Z. P., Hu, W. Q., Ren, H. Y., Tian, E., Zhao, Y., Lu, Q., Huang, X. X., Yang, P. G., Li, X., Wang, X., Kovács, A. L., Yu, L., and Zhang, H. (2010) *C. elegans* screen identifies autophagy genes specific to multicellular organisms. *Cell* **141,** 1042–1055
21. Lendahl, U., Zimmerman, L. B., and McKay, R. D. (1990) CNS stem cells express a new class of intermediate filament protein. *Cell* **60,** 585–595
22. Emery, B. (2010) Regulation of oligodendrocyte differentiation and myelination. *Science* **330,** 779–782
23. Mizushima, N., Yoshimori, T., and Levine, B. (2010) Methods in mamma-

lian autophagy research. *Cell* **140,** 313–326

24. Komatsu, M., Kurokawa, H., Waguri, S., Taguchi, K., Kobayashi, A., Ichimura, Y., Sou, Y. S., Ueno, I., Sakamoto, A., Tong, K. I., Kim, M., Nishito, Y., Iemura, S., Natsume, T., Ueno, T., Kominami, E., Motohashi, H., Tanaka, K., and Yamamoto, M (2010) The selective autophagy substrate p62 activates the stress responsive transcription factor Nrf2 through inactivation of Keap1. *Nat. Cell Biol.* **12,** 213–223
25. Lappe-Siefke, C., Goebbels, S., Gravel, M., Nicksch, E., Lee, J., Braun, P. E., Griffiths, I. R., and Nave, K. A. (2003) Disruption of Cnp1 uncouples oligodendroglial functions in axonal support and myelination. *Nat. Genet.* **33,** 366–374
26. Komatsu, M., Wang, Q. J., Holstein, G. R., Friedrich, V. L. Jr., Iwata, J., Kominami, E., Chait, B. T., Tanaka, K., and Yue, Z. (2007) Essential role for autophagy protein Atg7 in the maintenance of axonal homeostasis and the prevention of axonal degeneration. *Proc. Natl. Acad. Sci. U.S.A.* **104,** 14489–14494
27. Nishiyama, J., Miura, E., Mizushima, N., Watanabe, M., and Yuzaki, M. (2007) Aberrant membranes and double-membrane structures accumulate in the axons of Atg5-null Purkinje cells before neuronal death. *Autophagy* **3,** 591–596
28. Itakura, E., and Mizushima, N. (2010) Characterization of autophagosome formation site by a hierarchical analysis of mammalian Atg proteins. *Autophagy* **6,** 764–776
29. Budanov, A. V., and Karin, M. (2008) p53 target genes sestrin1 and sestrin2 connect genotoxic stress and mTOR signaling. *Cell* **134,** 451–460
30. Crighton, D., Wilkinson, S., O'Prey, J., Syed, N., Smith, P., Harrison, P. R., Gasco, M., Garrone, O., Crook, T., and Ryan, K. M. (2006) DRAM, a p53-induced modulator of autophagy, is critical for apoptosis. *Cell* **126,** 121–134